Structural properties and high-temperature spin and electronic transitions in $GdCoO_3$: Experiment and theory

Yu. S. Orlov,[1,2] L. A. Solovyov,[3] V. A. Dudnikov,[1] A. S. Fedorov,[1,2] A. A. Kuzubov,[2] N. V. Kazak,[1] V. N. Voronov,[1] S. N. Vereshchagin,[3] N. N. Shishkina,[3] N. S. Perov,[4] K. V. Lamonova,[5] R. Yu Babkin,[5] Yu. G. Pashkevich,[5] A. G. Anshits,[2,3] and S. G. Ovchinnikov[1,2,6,*]

[1]*L.V. Kirensky Institute of Physics, Siberian Branch, Russian Academy of Sciences, Akademgorodok 50/38, Krasnoyarsk, 660036, Russia*
[2]*Siberian Federal University, Krasnoyarsk, 660041, Russia*
[3]*Institute of Chemistry and Chemical Technology, Siberian Branch, Russian Academy of Sciences, Akademgorodok 50/24, Krasnoyarsk, 660049, Russia*
[4]*Faculty of Physics, M.V. Lomonosov Moscow State University, Moscow, GSP-1, Leninskie Gory, 1, bld. 2, 119991, Russia*
[5]*O.O. Galkin Donetsk Institute for Physics and Engineering, National Academy of Sciences of Ukraine, Donetsk, 83114, Ukraine*
[6]*M.F. Reshetnev Siberian State Aerospace University, Krasnoyarsk, 660014, Russia*

(Received 16 May 2013; revised manuscript received 24 August 2013; published 4 December 2013)

We have investigated the x-ray diffraction (XRD) structure, magnetic susceptibility, and heat capacity of $GdCoO_3$ in a wide temperature range. A model of phase separation of the low-spin (LS) and high-spin (HS) states has been proposed based on the analysis of XRD peak shape anomalies in the temperature range 200–800 K. From magnetic measurements we separated the HS Co^{3+} contribution and fitted it with the temperature-dependent spin gap. We found a smooth LS-HS crossover at $T = 800$ K. The possible contribution of the intermediate spin (IS) state to the thermodynamics is excluded by the calculation IS-LS excitation energy within the modified crystal-field approach. In the two-phase model, with HS/LS probabilities calculated from the found spin gap and the LS and HS volumes calculated by the DFT-GGA method, we were able to reproduce the temperature dependence of the unit-cell volume and thermal expansion. Thus, we conclude that in $GdCoO_3$ the main mechanism of the lattice expansion is not the conventional lattice anharmonicity, but the HS/LS fluctuations. The electronic structure has been calculated by the LDA + GTB method. At zero temperature, we have obtained the charge-transfer insulator with the charge gap $E_g = 0.5$ eV. The thermal population of the HS term results in the in-gap band formation inside the insulator gap and smooth insulator-metal transition at $T_{\mathrm{IMT}} = 780$ K. Heat-capacity measurements revealed a smooth maximum near the T_{IMT}.

DOI: 10.1103/PhysRevB.88.235105 PACS number(s): 71.27.+a

I. INTRODUCTION

Additionally to the intricate interplay between spin, charge, and orbital degrees of freedom in strongly correlated oxides, the rare-earth cobaltites $RCoO_3$ (R = La,Lu) reveal thermal fluctuations of the spin value.[1] These fluctuations have been studied in detail for $LaCoO_3$ with a long-standing controversy lasting from the 1950s.[2] While the ground state of the Co^{3+} ion is singlet (low spin, LS) the excited state may have either intermediate spin (IS, $S = 1$) or high spin (HS, $S = 2$). Thermal population of the excited magnetic states results in the spin-state transition. The signature for the onset of spin-state transition at $T_{\mathrm{onset}} \sim 35$ K for $LaCoO_3$ can be found in magnetic susceptibility,[3–5] heat capacity,[4,6] and thermal expansion.[3] The electronic spin resonance (ESR),[7] the x-ray absorption spectroscopy (XAS), and the x-ray magnetic circular dichroism[8] (XMCD) experiments prove that the lowest excited state is really the HS. Nevertheless, the $^5T_{2g}$ HS term is split by the spin-orbital interaction in the low-energy triplet with the total moment $J = 1$ and higher-energy sublevels with $J = 2$ and 3.[9] The multielectron LDA + GTB band-structure calculations for $LaCoO_3$ have shown that thermal excitation of the HS states results in the in-gap states formation, decreasing the charge excitation gap up to zero at $T = T_{\mathrm{IMT}}$.[10] The average Co^{3+} magnetic moment $J_{\mathrm{av}} = \langle J^2 \rangle^{1/2}$ strongly depends on temperature.[10] The value of $J_{\mathrm{av}} \approx 2$ at $T > 1000$ K while for $T = 300$ K $J_{\mathrm{av}} \approx 1$. This result explains why there are many indications for the IS from fitting the high-temperature paramagnetic susceptibility $\chi(T)$ by the Curie law and some other experimental data.

Substitution of smaller R^{3+} for R = La in $RCoO_3$ results in the chemical pressure effect and stabilization of the LS state due to increasing the value of the spin gap $\Delta_s = E_{\mathrm{HS}}$-$E_{\mathrm{LS}}$. This gap has been estimated for all R by fitting the temperature-dependent magnetic susceptibility[11] and by using the Berch-Murnaghan equations of state.[12] Both estimations for $GdCoO_3$ result in the spin-gap value $\Delta_s \approx 2200$–2300 K at zero temperature. The electronic phase diagram for $RCoO_3$ as a function of the R^{3+} ionic radius has been suggested based on the heat-capacity and magnetic susceptibility measurements.[13] Due to a very large thermal expansion, the growth of the lattice parameters and volume with heating is similar to the negative pressure and results in decreasing the spin gap up to $\Delta_s = 0$ at $T = T_S = 717$ K in $GdCoO_3$.[11] It means that the HS-LS crossover is expected at $T = T_S$. In the temperature interval $T_{\mathrm{onset}} < T < T_S$, there are strong HS-LS fluctuations. Due to the difference in the ionic radii of the HS and LS Co^{3+}, these fluctuations must be accompanied by strong distortions of the crystal lattice. We have found the evidence for such fluctuations in the anomalous peak asymmetry of the XRD patterns at 200 K $< T <$ 800 K. A very similar anomaly is revealed in the temperature dependence of the volume expansion coefficient $\Delta V/V\Delta T$ with the maximum at $T \sim 600$ K. This anomaly was found in Ref. 11 and is

 ©2013 American Physical Society

confirmed by our measurement. Due to the high temperature of our measurements, one should check whether the thermally excited IS states give contributions to the thermodynamics. We estimated the temperature dependence of the IS state energy and found that at $T = 800$ K the concentration of IS states was $n_{\mathrm{IS}} \sim 10^{-4}$, which might be considered negligible.

To clarify the origin of the anomalous thermal expansion and the XRD peak asymmetry, we have carried out *ab initio* calculations of the electronic and magnetic structure as well as equilibrium lattice parameters of three $GdCoO_3$ structures with different magnetic properties. Specifically, we calculated properties of three structures in a ferromagnetic state for different magnetic moments of Co atoms. To do it, the total magnetic moments of the unit cell ($Gd_4Co_4O_{12}$) were fixed to 28 μ_B (4 Gd ions with $S = \frac{7}{2}$ and nonmagnetic LS Co), 36 μ_B (IS Co with $S = 1$), and 44 μ_B (HS Co with $S = 2$). For all calculations, the projector augmented-wave method[14] (PAW) within the framework of the density-functional theory (DFT-GGA approach) and plane-wave basis were used, as implemented in the VASP software.[15,16] The electron-ion interaction was treated with ultrasoft Vanderbilt pseudopotentials.[17] The application of these pseudopotentials for the $GdCoO_3$ structure allows reducing the cutoff energy down to 400 eV. In these calculations, all f electrons of Gd atoms were treated as valence electrons. The exchange-correlation terms were considered via the Perdew-Berke-Ernzerhof form of the generalized gradient approximation (GGA).[18] The k-point samplings of the first Brillouin zone (1BZ) were chosen as $8 \times 8 \times 6$ according to the Monkhorst-Pack scheme.[19] All structures were relaxed until forces acting on all atoms became smaller than 0.01 eV/Å.

From the DFT-GGA, we have estimated the lattice parameters and unit-cell volumes at $T = 0$ for the HS, IS, and LS states. With known spin gap $\Delta_S(T)$, it is easy to calculate the HS (LS) fraction $n_{\mathrm{HS}}(T)$ [$n_{\mathrm{LS}}(T) = 1 - n_{\mathrm{HS}}$] and the average unit-cell volume $V = V_{\mathrm{HS}} n_{\mathrm{HS}} + V_{\mathrm{LS}} n_{\mathrm{LS}}$. It appears that for the HS and LS unit cells, the calculated lattice parameters a and c differ much less than the b parameters, in agreement with the experimental XRD data for the fluctuation region $T_{\mathrm{onset}} < T < T_S$. In the same model, we have calculated the thermal expansion coefficient. Its comparison with the experimentally measured coefficient reveals that the HS/LS fluctuation contribution to the thermal expansion in $GdCoO_3$ is much larger than the conventional lattice anharmonic one.

As for the electrical properties of $GdCoO_3$, both the resistivity[20,21] and heat-capacity[13] measurements have revealed the insulator-metal transition (IMT) around the T_{IMT}. The value of $T_{\mathrm{IMT}} = 700$ K (Ref. 13) and 725 K (Ref. 21). To calculate the $GdCoO_3$ electronic band structure and its change with temperature, one should go beyond the LDA/GGA approximations due to the problem of strong electron correlations. We have used the multielectron LDA + GTB (GTB means generalized tight-binding) method that has been developed to study the quasiparticle band structure in high-T_c cuprates[22,23] and recently extended to manganites[24] and cobaltites.[10] Our LDA + GTB calculations for $GdCoO_3$ have shown the appearance of the in-gap states inside the large (~0.5 eV) insulator gap of the LS $T = 0$ density of states (DOS). The in-gap states are induced by the HS thermal occupation. The more populated the HS state, the wider is the in-gap band, and finally it overlaps with the bottom of the conductivity band at some temperature $T_{\mathrm{IMT}} < T_S$. The insulator gap E_g continuously tends to zero as T tends to T_{IMT}, that is why the IMT can not be sharp. The smooth crossover between the insulator with decreasing small gap and the metal occurs in the interval 700–800 K. A wide peak of the heat capacity related to the IMT takes place in the $C_P(T)$ dependence measured for our samples and previously reported in Ref. 13.

The rest of the paper is organized in the following way. Section II gives the sample preparation and experimental method details. Section III contains the experimental data for the magnetic susceptibility, x-ray diffraction, and heat capacity in a wide temperature range. Analysis of the magnetic $\chi(T)$ measurements in Sec. IV allows obtaining the spin-gap temperature dependence $\Delta_S(T)$. In Sec. V, we present the results of the modified crystal-field approach to analyze the multielectron terms for HS, LS, and intermediate IS states and proves the irrelevance of the IS states for thermodynamics up to $T \sim 1000$ K. The XRD data for the unit cell and thermal expansion are discussed in the model of the HS and LS coexisting phases in Sec. VI. The LDA + GTB band structure and insulator-metal transition are discussed in Sec. VII. Section VIII contains conclusions.

II. SAMPLES PREPARATION AND EXPERIMENTAL METHODS

A. Samples preparation

We have prepared polycrystalline samples of $GdCoO_3$ by two different methods: the ceramic solid-state reaction technique and the sol-gel method. For the ceramic preparation, stoichiometric amounts of Gd_2O_3 and Co_3O_4 powders, all 99.9% purity, were thoroughly mixed and fired at 1100 °C. Then, the mixture was reground, pellets were pressed and sintered at 1100 °C for 24 h. This procedure was repeated three times. The materials used in the sol-gel synthesis were the gadolinium and cobalt heptahydrate nitrates and glycine (NH_2CH_2COOH); the purity of all reagents was >99.0%. The contents of metallic oxides and water quantity in the nitrates were preliminarily determined from thermogravimetric data using a Netzsch STA 449 C Jupiter instrument. To prepare the original gel, 5.00 g of $Gd(NO_3)_3$ $6H_2O$, 3.18 of $Co(NO_3)_2$ $6H_2O$, and 2.28 g of glycine were sequentially dissolved in 130 ml of distilled water and the resultant solution was stirred at 60 °C for 60 min. After that, the temperature was raised to 95 °C and kept at this level until water evaporation and gel formation. The gel was heated in the air with the rate 1 °C/min up to self-ignition at about 140 °C–170 °C. When the combustion process had been completed, the temperature was sharply increased up to 300 °C and held for 30 min. The resulting black powder was pressed in pellets at 3500 kg/cm^2 and the pellets were sintered in air at 1100 °C for 24 h.

The structure and magnetic properties of the samples obtained by the sol-gel and ceramic technologies were found to be similar; further, we will discuss mainly the data obtained with the ceramics sintered in the solid phase reaction. The heat capacity will be shown in the following for both types of samples.

B. Powder x-ray diffraction

The powder x-ray diffraction (PXRD) data for $GdCoO_3$ in the temperature interval 298–1273 K were collected on a PANalytical X'Pert PRO diffractometer equipped with a solid-state detector PIXcel using CoK_α radiation over the 2θ range 23°–157°. An Anton Paar HTK 1200N camera with the sample rotation and automated alignment was used. The low-temperature PXRD measurements at 213 and 133 K were carried out with a Bruker D8 ADVANCE powder diffractometer on CuK_α radiation with Vantec detector over the 2θ range 20°–105° in an Anton Paar TTK 450 camera. A powder sample of $GdCoO_3$ was prepared by grinding with octane in an agate mortar and packed into a flat sample holder for the PXRD measurements in the Bragg-Brentano geometry. The prepared sample was calcined for 2 h at 1273 K in the HTK before the measurements.

The full-profile crystal-structure analysis of $GdCoO_3$ was done using the Rietveld method[25] with the derivative difference minimization[26] (DDM) refinement. For the high-temperature data (298–1273 K), the lattice parameters, atomic coordinates, and anisotropic thermal factors were refined taking into account the preferred orientation, the anisotropic peak broadening, the sample surface roughness, and misalignment effects. Minor admixture phases (ca. 3%) of Co-Gd oxides and a gadolinium silicate oxide were included into the refined model. The low-temperature structures were refined isotropically due to the x-ray absorption problems.

C. Heat-capacity measurements

Heat-capacity data from 313 to 1073 K were obtained by the "ratio method" using a differential scanning calorimeter Netzsch STA Jupiter 449 C equipped with a special sample holder for C_p measurements. Three different runs under the same conditions (dynamic argon-oxygen atmosphere 20 vol.% O_2, the heating rate 10°/min) were carried out: (i) the baseline (empty platinum crucibles with perforated lids); (ii) a standard sapphire disk (40 mg) in the sample crucible; (iii) the sample of $GdCoO_3$ (70 mg, pressed as a disk of 6 mm in diameter) in the sample crucible. All runs were repeated three times to ensure the reproducibility of the data. The specific heat of the sample was then determined on the corrected Differential Scanning Calorimetry (DSC) curves according to Eq. (1):

$$C_p = \frac{m_{st}}{m_{sa}} \frac{\mathrm{DSC}_{sa} - \mathrm{DSC}_{bl}}{\mathrm{DSC}_{st} - \mathrm{DSC}_{bl}} C_{p,st}, \tag{1}$$

where $C_{p,st}$ is the tabulated specific heat of the standard at temperature T, m_{st}, m_{sa} are masses of the standard and the sample DSC_{sa}, (DSC_{st}, DSC_{bl}) is the value of DSC signal at temperature T from the sample (the standard, the baseline) curve.

D. Magnetization

The temperature dependence of magnetic moment was measured with a PPMS-9 (Physical Properties Measurement System; Quantum Design) between 2 and 300 K for samples subjected to zero-field-cooled (ZFC) or field-cooled (FC) regimes at magnetic fields 0.1 and 0.5 T. For the high-temperature range from 300 to 1000 K, a vibration magnetometer VSM 7407 (Lake Shore Cryotronics) was used. The relative measurement error was smaller then the linewidth in the experimental curves of the magnetic susceptibility.

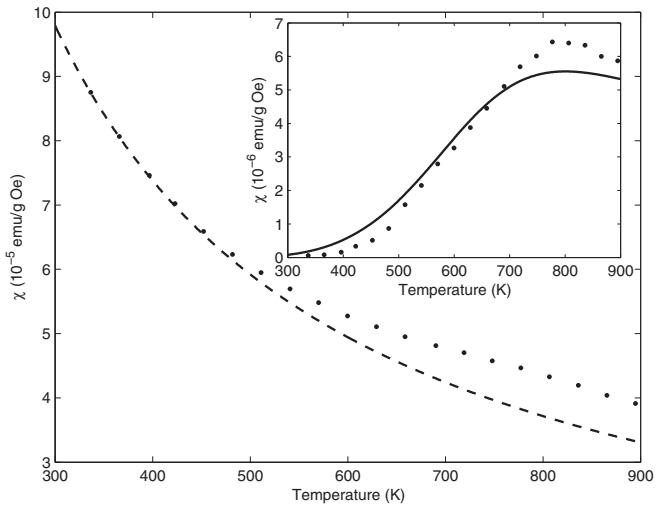

FIG. 1. Temperature dependence of $GdCoO_3$ magnetic susceptibility measured in a field 5 kOe (dark circles) and Gd^{3+} Curie-Weiss contribution (dashed curve). The inset shows the Co^{3+} ions susceptibility as the difference of the experimental and Gd ones (dark circles) and calculated (solid line) in Sec. IV, Eq. (3). Calculated Co^{3+} susceptibility obeys the Curie-Weiss law with the temperature-dependent effective magnetic moment [see Eq. (5)].

III. EXPERIMENTAL DATA

A. Magnetic susceptibility

The temperature dependence of susceptibility in a wide temperature range is shown in Fig. 1. The low-temperature region has been studied previously[27,28] and the inverse susceptibility beautifully fit the antiferromagnetic Curie-Weiss law $\chi_{\mathrm{Gd}} = \frac{g_{\mathrm{Gd}}^2 \mu_B^2 S(S+1)N}{3k_B(T-\Theta)}$, where N is the number of Gd^{3+} ions per unit volume, $S = \frac{7}{2}$, and $g_{\mathrm{Gd}} = 2$, with the asymptotic Curie temperature $\Theta_K \approx -5.3$ K, effective magnetic moment $\mu_{\mathrm{eff}} \approx 7.91\mu_B$ that is very close to the Gd^{+3} free ion $\mu_{\mathrm{eff}} = 7.94\mu_B$.

The Néel temperature of the antiferromagnetic Gd^{3+} spin ordering is equal to $T_N = 3.3$ K. Using the mean field expression for the Néel temperature in the Heisenberg model, we can estimate the Gd-Gd exchange interaction parameter $J_{\text{Gd-Gd}} = -0.11$ K. Subtracting the Gd Curie-Weiss magnetic susceptibility from the measured one, we have obtained the Co^{3+} susceptibility shown in the inset of Fig. 1. As expected, it is zero at low temperatures and increases at heating with a wide maximum around 800 K.

B. Powder x-ray diffraction data

The observed, calculated, and difference PXRD profiles after the DDM refinement of the $GdCoO_3$ crystal structure at 298 and 1273 K are shown in Fig. 2. The profile fit is nearly perfect up to the highest 2θ values, indicating a high quality of the refinement. The structure data for the whole studied temperature range are available in the Supplemental Material.[29]

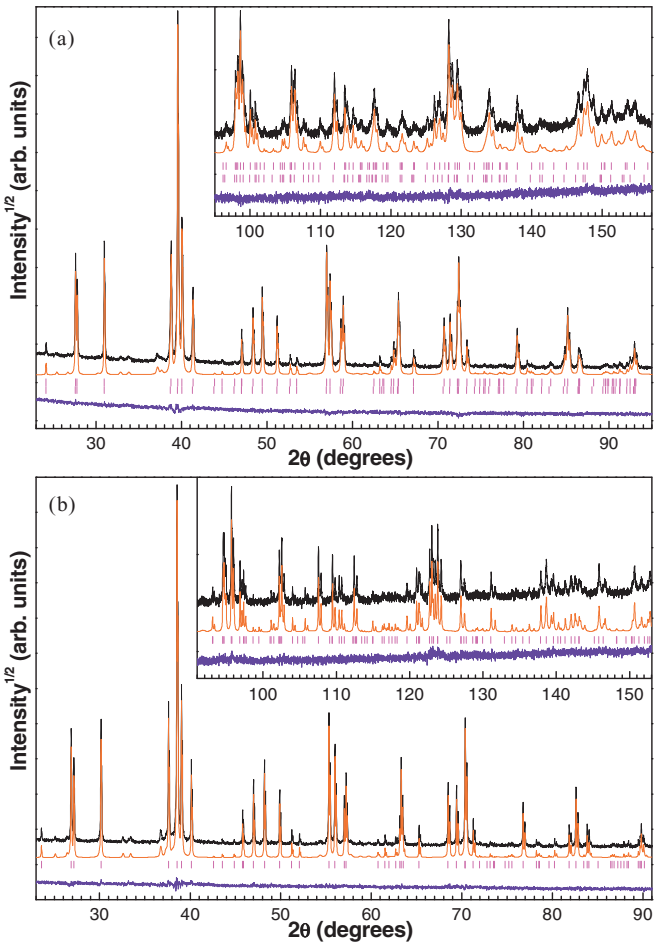

FIG. 2. (Color online) Observed (top, black), calculated (mid, red), and difference (bottom, blue) PXRD profiles after DDM refinement of $GdCoO_3$ crystal structure at 298 K (a) and 1273 K (b). The calculated peak positions of the main and the second phase are marked by ticks.

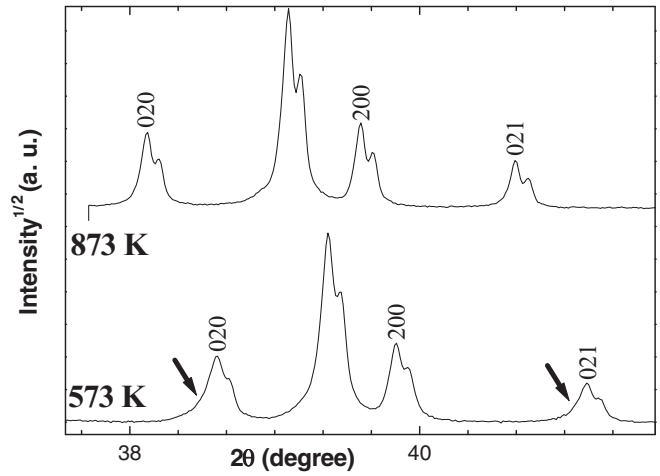

FIG. 3. Characteristic fragments of $GdCoO_3$ diffractogram at 573 and 873 K. The asymmetric peak broadening is shown by arrows for 573 K. For high temperature 873 K, the asymmetry is absent.

In the temperature range 200–800 K, a notable asymmetric *hkl*-dependent diffraction peak broadening was revealed, gradually disappearing at higher and lower temperatures. The PXRD pattern fragments demonstrating the *hkl*-dependent peak asymmetry are shown in Fig. 3. The respective peak shape evolution was reproducibly observed for repeated cooling and heating of the samples prepared by both the sol-gel and the ceramic methods. In Fig. 2, one may note that the diffraction peaks at 1273 K are substantially narrower than those at 298 K due to the asymmetric broadening shown in Fig. 3. The broadening is successfully modeled by the inclusion of the second phase, implying the presence of inhomogeneities within the crystals in the form of extended areas (domains) with different lattice parameters. These inhomogeneities may be related to a random spatial distribution of different spin states of Co in the crystal volume since the highest peak asymmetry is observed in the interval between 300 and 700 K where the expected probability of higher-spin states grows most rapidly (Fig. 9).The temperature dependencies of the lattice parameters, unit-cell volume, volume-expansion coefficient, and the refined second-phase fraction are shown in Fig. 4. The respective values calculated from the DFT-GGA optimized structure for the LS, IS, and HS models are also superimposed on the plots. It may be noted that in the low-temperature range up to 800 K, the refined unit-cell parameter b of the second phase is systematically higher than the first-phase value, while the remaining parameters a and c are nearly identical, indicating that the expanded-lattice domains are commensurable with the "normal" ones in the ac lattice plane and may be adjoined with each other by these planes. The relative difference between the DFT-optimized unit-cell parameters for the LS and the HS models is, similarly, the biggest for the lattice constant b, which additionally supports the relation of the observed structural features to the changes of the Co states.

The average values of the main interatomic distances and angles in the $GdCoO_3$ crystal structure after the DDM refinement are plotted versus temperature in Fig. 5. The observed dependencies demonstrate notable changes above 500 K analogously to the other characteristics of the material discussed in this work. The decrease of ⟨O-Co-O⟩ and ⟨Co-O-Co⟩ angles at higher temperatures points to the increased distortion and tilt of the CoO_6 octahedra in the structure. The DFT-optimized values demonstrate similar trends from the LS to the HS state. The average ⟨Co-O⟩ distances are close to those in the $LaCoO_3$ structure[30] up to 700 K, but become significantly increased at higher temperatures.

In Fig. 6(a), we compare the thermal dilatation in $LaCoO_3$ and $GdCoO_3$ crystals to demonstrate larger dilatation (e.g., the negative pressure) in $GdCoO_3$. To compare the Co-O bond length in $LaCoO_3$ and $GdCoO_3$, one should keep in mind the different symmetry of their lattices. Thus, all six bonds Co-O in $LaCoO_3$ are equal,[30] while in $GdCoO_3$ there are three pairs of unequal Co-O bonds. In Figs. 5 and 6(a), we show the average ⟨Co-O⟩ length with vertical bar indicating the difference between the minimal and maximal lengths. For $T < 600$ K, the difference of ⟨Co-O⟩ length for $GdCoO_3$ and $LaCoO_3$ is very small, while for $T > 600$ K the ⟨Co-O⟩ length in $GdCoO_3$ becomes remarkably larger than for $LaCoO_3$. Our *ab initio* calculations HS and LS bond lengths are given in Fig. 5 for $GdCoO_3$; they are larger than the corresponding

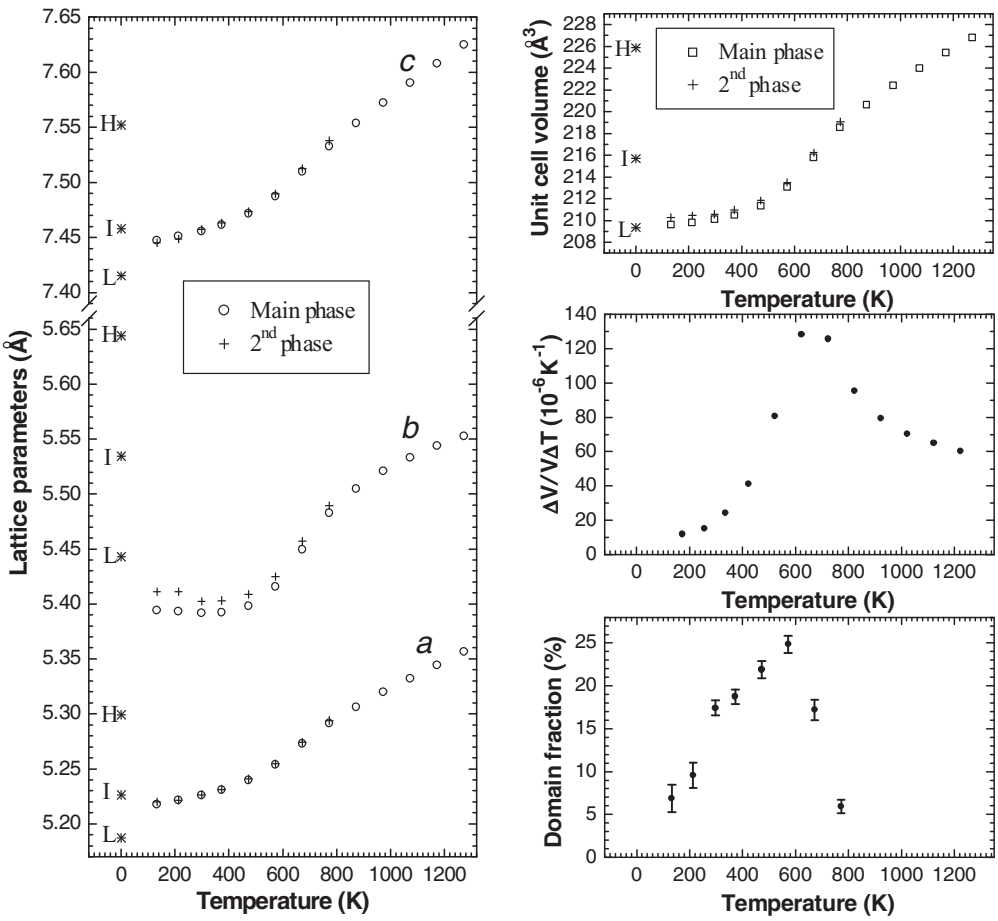

FIG. 4. Temperature dependencies of lattice parameters, unit-cell volume, volume-expansion coefficient, and expanded lattice domain (second phase) fraction for $GdCoO_3$. The values calculated from the DFT-optimized structure for the LS, IS, and HS models at $T = 0$ are marked as L*, I*, and H*, respectively.

values for $LaCoO_3$. Indeed, we have obtained the Co-O length (in Å): 1.915 (LS) and 1.923 (HS) for $LaCoO_3$ and 1.938 (LS) and 2.008 (HS) for $GdCoO_3$. The low-spin lengths in $LaCoO_3$ and $GdCoO_3$ do not differ much, while the high-spin data are strongly different. It explains the different high-temperature behavior of two oxides in Fig. 6(a). Nevertheless, for all temperatures the concentration of high-spin state $n_{HS}(T)$ for $LaCoO_3$ is larger than for $GdCoO_3$ just because the smallest spin gap is in $LaCoO_3$.[11] The CoO_6 octahedra in $GdCoO_3$ undergo temperature-induced high-symmetry distortions such as breathing mode, which are described by the normal coordinate Q_1, also the low-symmetry distortions such as rhombic (or Yahn-Teller, Q_2 and Q_3) and trigonal (Q_4, Q_5, Q_6) ones. The normal coordinates Q_α ($\alpha = 1, 2, \ldots, 3N - 3$; N, number of ligands) are linear combinations of the Cartesian coordinates, classified according to the irreducible representations of the coordination complex symmetry. In that case, it is the symmetry group of the octahedron O_h (see Table I). The temperature dependence of the most significant Q_α amplitudes is shown in Fig. 6(b). Apparently, the full-symmetric distortion Q_1 has a decisive influence on the isotropic high-temperature expansion of $GdCoO_3$ at $T > 600$ K. However, in the temperature range 133 K $< T <$ 600 K, the high-symmetry (isotropic) contribution Q_1 and low-symmetry (anisotropic) Q_3 and Q_5 contributions are comparable.

C. Heat capacity

Figure 13 shows temperature dependence of the calculated insulator gap and the measured heat capacity (C_P) of the $GdCoO_3$ samples prepared by two different methods. Both samples exhibit a wide peak of C_P with a maximum at 706 K. The observed deviation between the samples does not exceed 4% and lies within the experimental error of the method used. The position of the peak and the magnitude of C_P values for both samples are consistent with the data presented previously.[13]

IV. ANALYSIS OF THE MAGNETIC SUSCEPTIBILITY IN A WIDE TEMPERATURE RANGE

The total magnetization of $GdCoO_3$ can be presented as the sum of two terms: $M_{GdCoO_3} = M_{Gd} + M_{Co}$, where M_{Gd} and M_{Co} are the magnetizations of gadolinium and cobalt ions, respectively. To describe the contribution of Co^{3+} ions to the total magnetization of $GdCoO_3$, we consider the energy levels of Co^{3+} ions in the crystal field allowing for the spin-orbit interaction [Fig. 10(b)]. The ground term is represented by

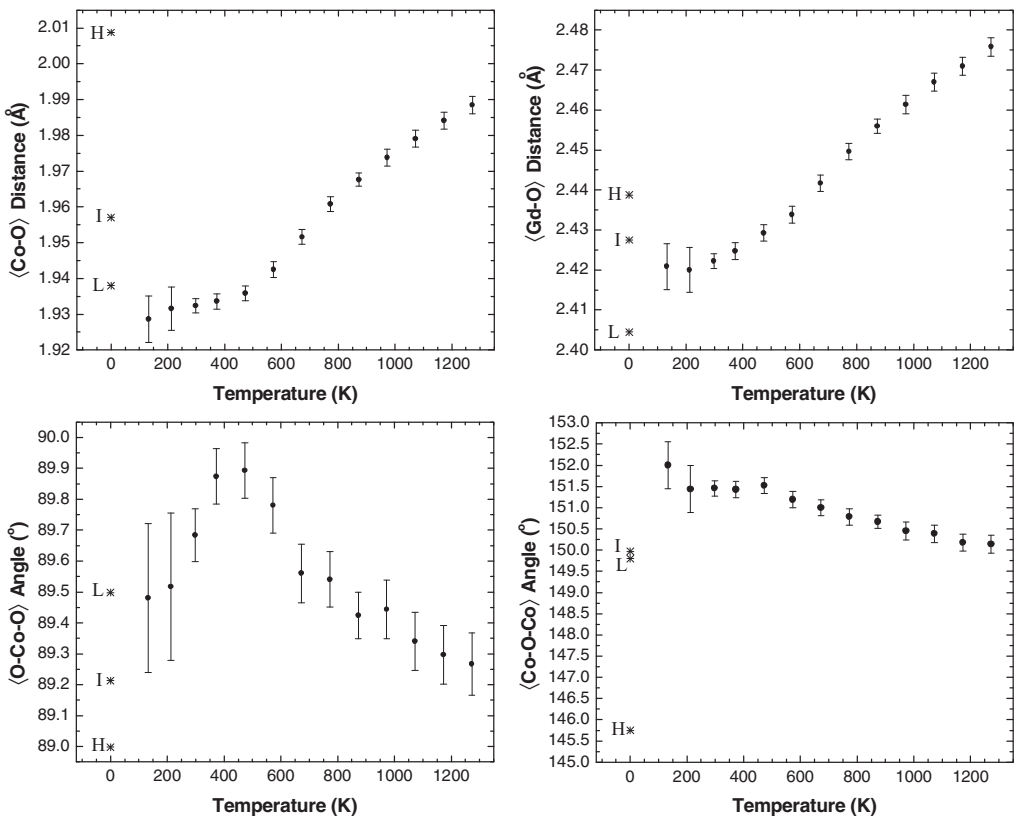

FIG. 5. Temperature dependencies of average distances and angles in $GdCoO_3$ crystal structure. The values calculated from the DFT-optimized structure for the LS, IS, and HS models at $T = 0$ are marked as L*, I*, and H*, respectively.

low-spin singlet $^1A_1$ separated from triplet sublevel $\tilde{J} = 1$ of high-spin state $^5T_{2g}$ by spin gap Δ_S. At $\Delta_S = 150$ K, the term positions correspond to the data obtained for $LaCoO_3$ in Refs. 7, 9, and 31. The substitution of a certain rare-earth ion with a smaller ionic radius for lanthanum leads to the chemical pressure, which is equivalent to an external pressure. It is caused by the record compressibility of the Co-O bond in cobalt-oxide compounds.[32] This substitution results in additional stabilization of a low-spin state, in other words, in an increase of the spin gap.

The partition function of Co^{3+} ions of one mole of $GdCoO_3$ within the energy levels scheme of Fig. 10(b) takes the form

$$\begin{aligned} Z = \{&1 + e^{-\beta\Delta_S} + 2e^{-\beta\Delta_S} ch(y_1) + e^{-\beta(\Delta_S+2\tilde{\lambda})} \\ &+ 2e^{-\beta(\Delta_S+2\tilde{\lambda})}[ch(y_2') + ch(y_2'')] \\ &+ 3e^{-\beta(\Delta_S+5\tilde{\lambda})} + 2e^{-\beta(\Delta_S+5\tilde{\lambda})}[ch(y_3') + ch(y_3'')]\}^{N_A}, \end{aligned} \tag{2}$$

where $y_1 = \beta(g_1\mu_B\tilde{B} + 2Jz\langle\mu\rangle)$, y_2', y_2'', y_3', and y_3'' are obtained from y_1 by replacing g_1 by g_2', g_2'', g_3', and g_3'', respectively. N_A is the Avogadro number, $\tilde{\lambda}$ is the effective spin-orbit interaction constant, $\tilde{B}$ is the applied magnetic field, k_B is the Boltzmann constant, $\beta = 1/k_BT$, and μ_B is the Bohr magneton. The Lande factors are $g_1 = 3.4$ for triplet $\tilde{J} = 1$, $g_2' = 3.1$, and $g_2'' = 1.8$ for quintet $\tilde{J} = 2$ and $g_3' = 0.6$, $g_3'' = 1.7$ for septet $\tilde{J} = 3$, $\tilde{\lambda} = 185$ K.[9] The magnetization $M = N_A\langle\mu\rangle$ in terms of the mean magnetic moment per spin $\langle\mu\rangle$ is obtained by differentiation of $\ln Z$ in the usual way. Antiferromagnetic interaction $J_{\text{Co-Co}}$ between Co ions have previously been introduced in model calculations for the magnetic susceptibility of $LaCoO_3$,[31,33] and we adopt the similar approach for $GdCoO_3$. According to Ref. 31, $J_{\text{Co-Co}} = -27.5$ K. We also have included the Gd-Co exchange interaction in the fitting procedure of the high-T magnetic susceptibility. The parameter $J_{\text{Gd-Co}}$ was estimated to be less than 1 K. For high-T Co susceptibility, its contribution is negligibly small. It is of the same order as $J_{\text{Gd-Gd}} = -0.11$ K (see Sec. III above). Nevertheless, it is irrelevant for the low-T Gd magnetization also due to zero magnetic moment of the LS Co^{3+} ion. That is why we neglect the $J_{\text{Gd-Co}}$ below.

Assuming that only the nearest-neighbor interactions need to be considered and using the mean field approximation, one may obtain an exchange contribution to the effective field for the split HS triplet, quintet, and septet states given by $\varepsilon_{\text{exch}} = 2J\langle\mu\rangle zm_S$, where $J = J_{\text{Co-Co}}$ is the exchange coupling, z the coordination number. Introduction of the antiferromagnetic correlation energy leads to the self-consistent expression for the magnetization per spin

$$\begin{aligned} \frac{\langle\mu\rangle}{\mu_B} = \exp(-\beta\Delta_S)Z^{-1}\{&2\sinh(y_1)g_1 \\ &+ 2\exp(-2\tilde{\lambda}\beta)[\sinh(y_2')g_2' + \sinh(y_2'')g_2''] \\ &+ 2\exp(-5\tilde{\lambda}\beta)[\sinh(y_3')g_3' + \sinh(y_3'')g_3'']\}. \end{aligned} \tag{3}$$

If we neglect the small spin-orbital interaction, all HS sublevels will join together into one HS term with spin $S = 2$, orbital moment $L = 1$, and total degeneracy $g_{\text{HS}} = 15$, and Eq. (3)

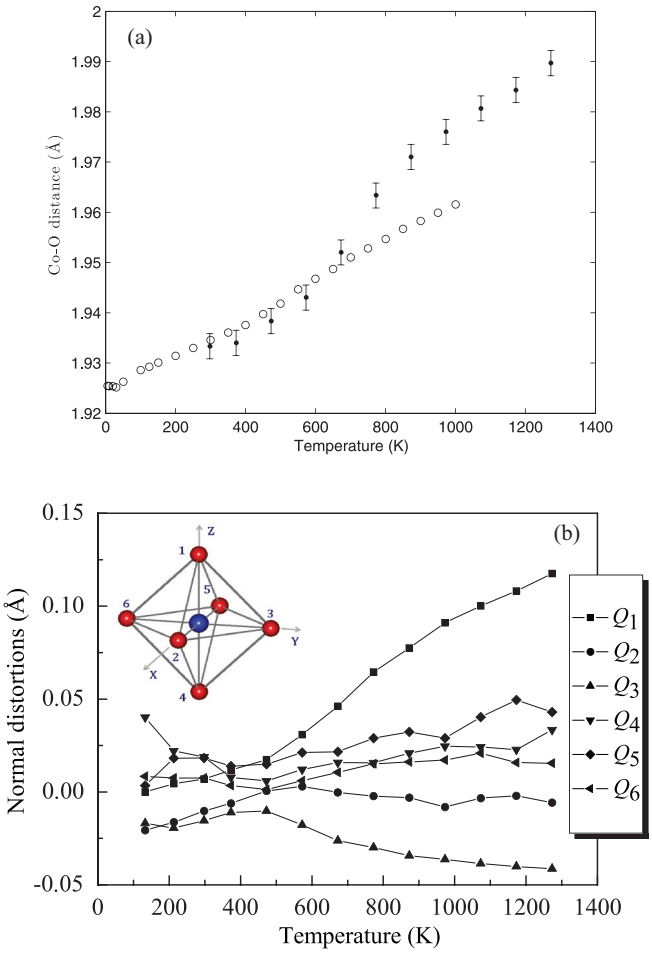

FIG. 6. (Color online) Temperature dependencies (a) of the Co-O distance in $LaCoO_3$ [circles (Ref. 30)] and $GdCoO_3$ (points, data from Fig. 5), (b) of the calculated most significant $[CoO_6]^{9-}$ distortions. The inset shows a model octahedral complex. The numbering of ligands corresponds to the one in Ref. 46.

TABLE I. Normal coordinates of the $[MO_6]$ octahedral complex, expressed in Cartesian coordinates shifts.

Normal coordinates	Type of symmetry	Expression through the Cartesian displacement
Q_1	A_{1g}	$(x_2 - x_5 + y_3 - y_6 + z_1 - z_4)/\sqrt{6}$
Q_2	E_g	$(x_2 - x_5 - y_3 + y_6)/2$
Q_3	E_g	$(x_2 - x_5 - y_3 + y_6)/2$
Q_4	T_{2g}	$(z_3 - z_6 + y_1 - y_4)/2$
Q_5	T_{2g}	$(x_1 - x_4 + z_2 - z_5)/2$
Q_6	T_{2g}	$(y_2 - y_5 + x_3 - x_6)/2$
Q_7	T'_{1u}	$(x_1 + x_3 + x_4 + x_6)/2$
Q_8	T'_{1u}	$(y_1 + y_2 + y_4 + y_5)/2$
Q_9	T'_{1u}	$(z_2 + z_3 + z_5 + z_6)/2$
Q_{10}	T''_{1u}	$(x_2 + x_5)/\sqrt{2}$
Q_{11}	T''_{1u}	$(y_3 + y_6)/\sqrt{2}$
Q_{12}	T''_{1u}	$(z_1 + z_4)/\sqrt{2}$
Q_{13}	T''_{2u}	$(x_3 + x_6 - x_1 - x_4)/2$
Q_{14}	T''_{2u}	$(y_1 + y_4 - y_2 - y_5)/2$
Q_{15}	T''_{2u}	$(z_2 + z_5 - z_3 - z_6)/2$

takes the form

$$\frac{\langle\mu\rangle}{g\mu_B} = \frac{6\,(\sinh x + 2\sinh 2x)}{3 + \exp(\beta\Delta) + 6\,(\cosh x + \cosh 2x)}, \tag{4}$$

where $x = g\mu_B B\beta + Jz\,\langle\mu\rangle\,\beta$, $\beta = 1/k_B T$, and $g = 2$ is purely spin Lande factor. Then, the expression for the molar magnetic susceptibility of cobalt may be obtained in the Curie-Weiss form with the effective Curie "constant" and temperature

$$\chi_{\rm Co} = N_A \frac{\partial\,\langle\mu\rangle}{\partial B} = N_A \frac{C_{\rm eff}}{3k_B(T - \Theta_{\rm eff})}. \tag{5}$$

$C_{\rm eff} = g^2\mu_B^2 S\,(S+1)\,n_{\rm HS}$ is the effective Curie constant, depending on the population of high-spin state

$$n_{\rm HS} = \frac{g_{\rm HS}\exp(-\Delta_S/k_B T)}{1 + g_{\rm HS}\exp(-\Delta_S/k_B T)}, \tag{6}$$

where $g_{\rm HS} = 15$ is the degree of degeneracy of the $^5T_{2g}$ term. The effective Curie temperature is equal to $\Theta_{\rm eff} = \frac{J_{\rm Co\text{-}Co} z S(S+1)}{3k_B} n_{\rm HS}$. As can be seen from these expressions, the effective magnetic moment of cobalt and the Curie temperature depends on temperature because the excited magnetic state HS is separated from the nonmagnetic LS by the energy gap Δ_S. The temperature-dependent spin gap determines the Co^{3+} magnetic susceptibility. At low T, the concentration $n_{\rm HS}$ goes to zero and the magnetic susceptibility tends to zero also.

A prominent feature of the rare-earth cobaltites is their anomalous thermal expansion. According to Ref. 11, the temperature dependencies of the thermal expansion coefficient for LnCoO$_3$ with Ln = La, Dy, Sm, Pr, Y, Gd, and Nd are not monotonic and have a maximum whose position correlates with features in the magnetic susceptibility and conductivity. The thermal expansion of the sample leads to an increase in Co-O bond length, and hence to a reduction of the spin gap Δ_S since the latter is determined by the crystal field $10Dq$. The analytic expression for the temperature dependence of the spin gap was proposed for a number of rare-earth cobaltites.[11] The energy $\Delta_S(T)$ was fitted by a power function

$$\Delta_S(T) = \Delta_0\left[1 - \left(\frac{T}{T_S}\right)^n\right], \tag{7}$$

where Δ_0 is the spin gap at $T = 0$ K, T_S is the temperature where $\Delta_S(T_S) = 0$. T_S and n are the fitting parameters. According to Ref. 11 for $GdCoO_3$ $\Delta_0 = 2260$ K, $T_S = 717$ K, $n = 3.39$. Recent estimation of the spin gap for $GdCoO_3$ at low temperatures using the Birch-Murnaghan equation[34] results in $\Delta_S \approx 2000$ K, which agrees qualitatively with the data.[11] The solid line in the inset to Fig. 1 shows the results of calculating $\chi_{\rm Co}$ using the Eq. (3) with $\Delta_0 = 2300$ K, $T_S = 800$ K, and $n = 4$. Parameters Δ_0, T_S, n have been found by fitting the temperature-dependent Co^{3+} susceptibility both in Ref. 11 and here. Qualitatively, they are similar. The quantitative difference results from different assumptions for the excited magnetic state. In our paper, it is the HS term with degeneracy $g_{\rm HS} = 15$, while the IS state with $S = 1$ was assumed in the model.[11] Figure 7(b) shows the change of the spin gap with increasing temperature for these values.

At the end of this section, we would like to mention the difference between the expression and arguments presented here from those used in our previous work.[34] In Ref. 34,

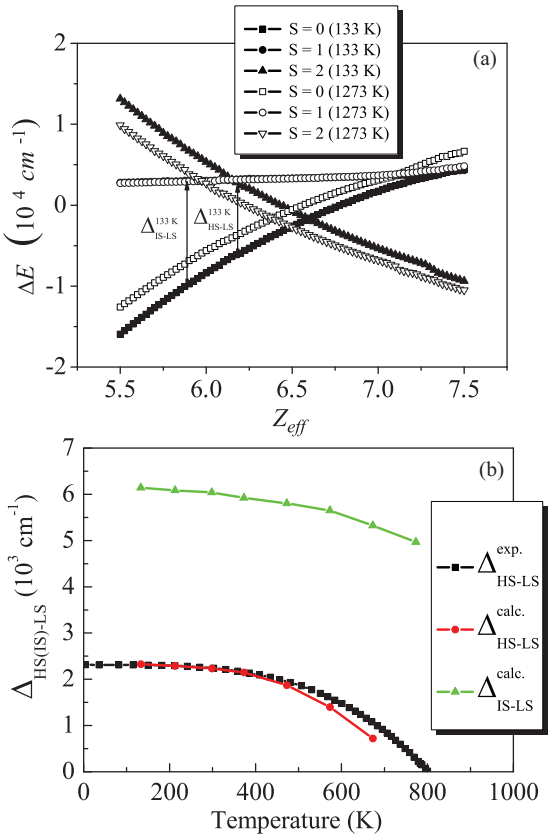

FIG. 7. (Color online) (a) The dependence of Co^{3+} energy levels on the effective nuclear charge Z_{eff}; (b) the temperature dependence of the spin state gap $\Delta^{\text{exp}}_{\text{HS-LS}}$, obtained by fitting experimental susceptibility with Eq. (7), and those theoretically calculated by the MCFA: $\Delta^{\text{calc.}}_{\text{HS-LS}}$ and $\Delta^{\text{calc.}}_{\text{IS-LS}}$.

the spin gap is found at $T = 0$ K and has been assumed temperature independent. Here, the anomalous temperature dependence of the unit-cell volume and other structural characteristics induced us to treat the spin gap as given by Eq. (7). Thus, the LS state was considered as stable in Ref. 34, while here we found the LS-HS crossover with heating. Moreover, the Co-Co exchange is included here and was omitted in Ref. 34. This interaction results in the self-consistency Eq. (3) for susceptibility, while in Ref. 34 Co spins have been treated as independent.

V. HIGH-TO-LOW SPIN EVOLUTION WITHIN THE MODIFIED CRYSTAL-FIELD THEORY

In this section, we have investigated the electronic spectra of Co^{3+} ions with regular and arbitrarily distorted CoO_6 octahedral complexes, within the modified crystal-field approach (MCFA). The basic MCFA statements are outlined in Refs. 35–37. Here, we note only that (i) the basis set of the eigenfunctions corresponding to the specific $3d^n$ configuration includes the finite number of orthogonal antisymmetric many-electron wave functions, composed of the hydrogenlike functions with effective nuclear charge Z_{eff} as the only variable parameter; (ii) the Born-Oppenheimer approximation is inherently assumed, while many-electron wave functions are the functions of ligand nuclear coordinates as the variable parameters; (iii) the spin-orbit interactions are taken into account.

The electronic configuration of trivalent cobalt is $3d^6$ and it allows three different spin states, namely, the high-spin state (HS, $S = 2$), the state with the intermediate spin (IS, $S = 1$), and the low-spin state (LS, $S = 0$). We have calculated the energy levels (energy diagrams) for Co^{3+} ions in oxygen octahedral surrounding with the coordinates taken from the XRD data for different temperatures and plotted ones [Fig. 7(a)] similarly to the Tanabe-Sugano diagrams.[38] However, unlike traditional Tanabe-Sugano diagrams, we used the effective nuclear charge Z_{eff} instead of the crystal-field splitting Δ_{CF} as the variable parameter. The value Δ_{CF} is the experimentally measurable one and it depends on several parameters of coordination complex: the ligand charges, the effective nuclear charge, as well as the set of ligand coordinates. If one varies Δ_{CF}, it is impossible to determine the cause of the energy spectrum rearrangement because each of the above-mentioned parameters has a different effect on the crystal-field splitting. The MCFA allows calculation with arbitrary symmetry of coordination complexes and arbitrary set of ligand charges, which significantly expands the applicability of the method. The variable Z_{eff} allows considering implicitly the covalence degree of "metal-ligand" bond. As an example, in Fig. 7(a) we presented the lowest-energy levels of the Co^{3+} ion, which correspond to the different spin states at 298 and 1273 K.

First of all, we note that the energy levels are rearranged with the temperature change [Fig. 7(a)]. The distance between the high- and low-spin levels, i.e., the spin gap $\Delta_{\text{HS-LS}} = E_{\text{HS}}\text{-}E_{\text{LS}}$ found from the energy diagrams, decrease with increasing temperature [Fig. 7(b)]. The HS $\leftrightarrow$ LS crossover point shifts to lower Z_{eff} with increasing temperature up to 1273 K. Meanwhile, the intermediate-spin level does not react to the temperature changing [Fig. 7(a)]. However, the spin gap $\Delta_{\text{IS-LS}} = E_{\text{IS}}\text{-}E_{\text{LS}}$ is temperature dependent due to the temperature dependence of the low-spin state. The energy separation of the IS state from the LS one is shown in Fig. 7(b) also. It is clear that for the whole temperature interval, the IS has too large energy to be thermally populated. For this reason, we did not include the IS term in the partition function (2).

To visualize the behavior of the Co^{3+} spin subsystem under the influence of a homogeneous expansion, we built the spin-state diagram $\langle S^2\rangle = f(Z_{\text{eff}}, Q_1)$ (Fig. 8). The spin-state diagram represents the average spin square of trivalent cobalt ion as a function of effective nuclear charge Z_{eff}, and homogeneous expansion of $[CoO_6]$ complex Q_1, at fixed ligand charge values. It is seen that only high- and low-spin states are possible and the HS $\leftrightarrow$ LS transition line is not narrow. Comparing the calculated spin gap $\Delta_{\text{HS-LS}} = E_{\text{HS}}\text{-}E_{\text{LS}}$ with the experimental temperature-dependent spin gap [Fig. 7(b)], we have found the temperature dependence of the effective charge $Z_{\text{eff}}(T)$ in $GdCoO_3$. After that, knowing the dependence of the homogeneous expansion on temperature [Fig. 6(b)], we can obtain the dependence of the effective nuclear charge on Q_1, i.e., the $Z_{\text{eff}}(Q_1)$ trajectory (green line) in the spin-state diagram $\langle S^2\rangle = f(Z_{\text{eff}}, Q_1)$ (Fig. 8). Hence, one can expect that the spin transition starts when $Q_1 = 0.041$ and ends at $Q_1 = 0.051$, which corresponds to the onset temperature 650 K and the final one 700 K. This value for the

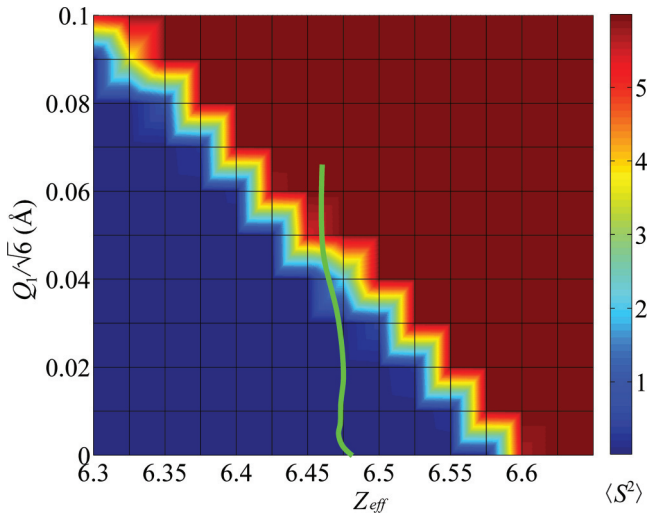

FIG. 8. (Color online) Spin-state diagram $\langle S^2 \rangle = f(Z_{\rm eff}, Q_1)$, calculated by MCFA, for the $[CoO_6]$ coordination complex under the breathing-mode expansion. The green line represents the $Z_{\rm eff}(Q_1)$ dependence. For each temperature value, there is a point $(Z_{\rm eff}, Q_1)$ at this diagram. Variation of temperature results in moving along the $Z_{\rm eff}(Q_1)$ trajectory.

spin crossover temperature is about 15% lower than the $T_S =$ 800 K found above from susceptibility fitting. Nevertheless, the difference is not so large for a qualitative agreement. The main reason for the underestimated spin crossover temperature is the restriction of homogeneous expansion in the spin-state diagram. In general, all normal coordinates determine the spin state $\langle S^2 \rangle = f(Z_{\rm eff}, Q_1, Q_2, \ldots, Q_{3N-3})$ and the neglect of all but Q_1 mode results in the deviation of calculated T_S within the MCFA from the experimental value.

VI. TWO-PHASE MODEL FOR STRUCTURAL PROPERTIES

At finite temperature, each Co^{3+} ion may be in the HS state with a probability $n_{\rm HS}(T)$ and in the LS state with $n_{\rm LS}(T)$. As shown above, the HS and LS states have the same symmetry with different unit-cell volumes $V_{\rm HS}$ and $V_{\rm LS}$ and lattice parameters. The unit-cell volumes are calculated *ab initio* within the DFT-GGA at $T = 0$, $V_{\rm HS}(0) = 225.87A^3$, $V_{\rm LS}(0) = 209.35A^3$. As was mentioned in the Introduction, the DFT-GGA calculation for the HS state was carried out for a hypothetical ferromagnetic (FM) $GdCoO_3$. There is no way to calculate the HS paramagnetic (PM) state within the conventional DFT theory. Thus, we have $V_{\rm HS}^{\rm (FM)} = 225.87A^3$ at $T = 0$. If to examine attentively the experimental points for the unit-cell volume $V(T)$ in Fig. 4 at $T = 1200$ K where $GdCoO_3$ is, obviously, in the PM state, the measured $V(T) \approx V_{\rm HS}^{\rm (FM)}(0)$ and there is now room for thermal expansion. It is clear that the calculated value is overestimated. Thus, we may conclude that the volume $V_{\rm HS}^{\rm (PM)}(0)$ in the PM state has to be smaller. The physical reason why it should be smaller is the magnetostriction. For example, in invar alloy the volume decrease with heating (and magnetization decreasing) is so large that it compensates the lattice thermal expansion. Of course, the magnetostriction is material dependent. Thus, we have a ground to assume that $V_{\rm HS}^{\rm PM}(0) < V_{\rm HS}^{\rm FM}(0)$. We consider $V_{\rm HS}(0)$ below as a fitting parameter.

Due to the lattice anharmonicity at finite T one can write

$$V_{\rm HS}(T) = V_{\rm HS}(0)(1 + \alpha_{\rm HS}T), \quad V_{\rm LS}(T) = V_{\rm LS}(0)(1 + \alpha_{\rm LS}T), \tag{8}$$

where $\alpha_{\rm HS}$ and $\alpha_{\rm LS}$ are the lattice contributions to the thermal expansion. For a random mixture of two phases in the virtual crystal approximation, we can write

$$V(T) = V_{\rm HS}(T)n_{\rm HS}(T) + V_{\rm LS}(T)n_{\rm LS}(T). \tag{9}$$

We introduce a spin fluctuation contribution

$$V_S(T) = V_{\rm HS}(0)n_{\rm HS}(T) + V_{\rm LS}(0)n_{\rm LS}(T), \tag{10}$$

that may be calculated independently of structural data. Then, the unit-cell volume may be written as

$$V(T) = V_S(T) + [V_{\rm HS}(0)n_{\rm HS}(T)\alpha_{\rm HS} + V_{\rm LS}(0)n_{\rm LS}(T)\alpha_{\rm LS}]\,T. \tag{11}$$

The temperature dependence of the $n_{\rm HS}(T)$ and $n_{\rm LS}(T)$ are determined by the spin gap $\Delta_S(T)$ given by Eq. (4) [see Fig. 9(a)]. The experimental $V(T)$ and calculated spin fluctuation value $V_S(T)$ are shown in Fig. 9(b). Here, we used the value $V_{\rm HS}(0) = 221.35A^3$. The main difference at high T is due to the lattice contribution. While $V_S(T)$ saturates at

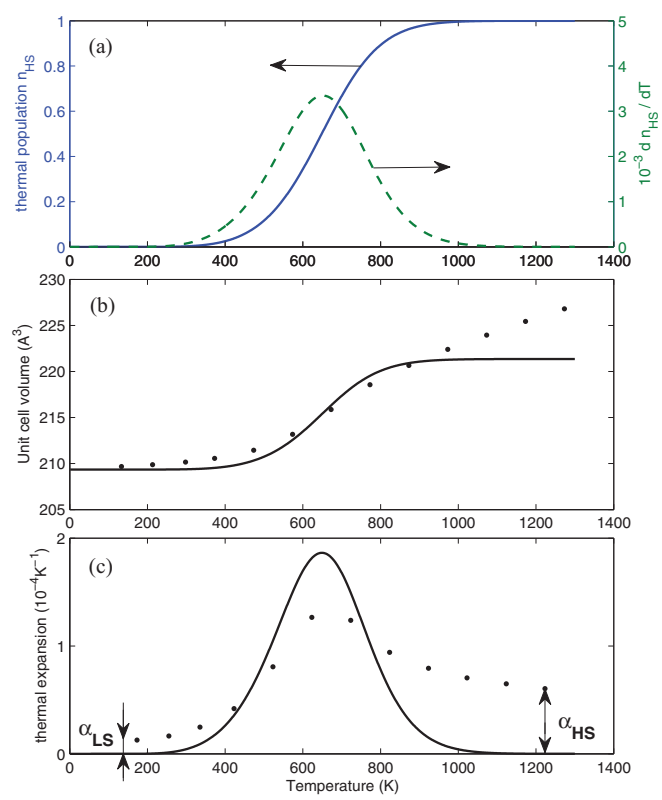

FIG. 9. (Color online) HS and LS coexistence model for crystal volume and thermal expansion given by Eqs. (8)–(12). HS concentration and its temperature derivative (a), unit-cell volume (b), thermal-expansion coefficient with lattice contributions LS at low T and HS at high T (c). The experimental data in (b) and (c) are shown by points, while solid lines denote calculated values.

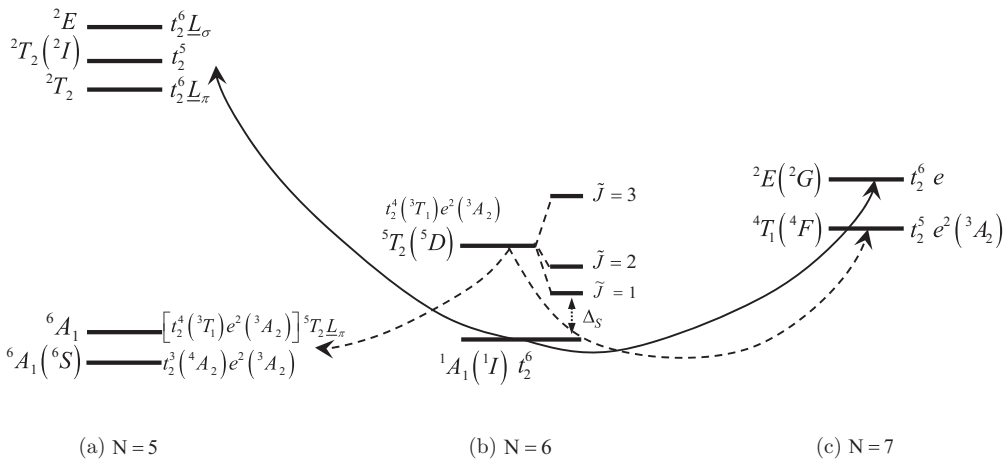

FIG. 10. Multielectron terms of CoO_6 cluster with five (a), six (b), and seven (c) electrons above the configuration $d^0(\mathrm{Co})p^6(\mathrm{O})$. For stoichiometric $GdCoO_3$ at $T = 0$, only the lowest $d^{61}A_1$ term LS is occupied, all other terms unoccupied. A set of Co^{3+} HS states split by spin-orbital interaction is above the LS term with the spin gap $\Delta_S = E_{\mathrm{HS}}$-$E_{\mathrm{LS}}$. Electron addition $d^6 \to d^7$ excitations forming the bottom of the conduction band and electron removal $d^6 \to d^5$ excitations forming the top of valence band are shown by solid lines. The dashed lines indicate the excitations responsible for the formation of in-gap states upon the HS thermal population.

$T \sim 1000$ K where $n_{\mathrm{HS}} \to 1$, $n_{\mathrm{LS}} \to 0$, the lattice anharmonicity results in the linear T contribution.

The linear expansion coefficient is given by

$$\alpha = \frac{1}{V}\frac{dV}{dT} = \alpha_S + \alpha_{\mathrm{latt}}, \quad \alpha_S = \frac{\partial n_{\mathrm{HS}}}{\partial T}\frac{V_{\mathrm{HS}}(0) - V_{\mathrm{LS}}(0)}{V(T)}. \tag{12}$$

The spin fluctuation contribution α_S as well as the HS domain fraction in the XRD data (Fig. 4) is determined mainly by the derivative $\partial n_{\mathrm{HS}}/\partial T$ shown in Fig. 9(a). The comparison of the measured parameter α and calculated value α_{S} in Fig. 9(c) allows estimating the lattice contribution at high T. Because $n_{\mathrm{HS}} \to 1$ at $T \sim 1000$ K, one has $\alpha_{\mathrm{latt}} = \alpha_{\mathrm{HS}}$. From Fig. 9(c), we get $\alpha_{\mathrm{HS}} \approx 5 \times 10^{-5} K^{-1}$. Similarly, at low $T \sim 100$ K, $n_{\mathrm{HS}} \to 0$ and the total lattice contribution is determined by the LS state. From Fig. 10(c) at low T we obtain $\alpha_{\mathrm{LS}} \approx 10^{-5} K^{-1}$. These values are typical for lattice anharmonicity; the HS contribution is large due to the largest ionic radius.

Thus, the virtual crystal approach allows understanding the volume-expansion peculiarities in $GdCoO_3$ at least qualitatively, implying the spin fluctuation mechanism to be dominant in a wide temperature range 77 K $< T <$ 800 K. The small quantitative disagreement between $V(T)$ and $V_S(T)$ in the intermediate temperature range results either from the incompleteness of the virtual crystal approximation or from an insufficient accuracy in the spin-gap fitting from magnetic data and the $V_{\mathrm{HS}}(0)$ estimation.

VII. TEMPERATURE-DEPENDENT ELECTRONIC STRUCTURE OF $GdCoO_3$ WITHIN THE LDA + GTB APPROACH

One of the interesting specific features of perovskitelike rare-earth $LnCoO_3$ cobaltites is a smooth insulator-metal transition occurring when the temperature increases. The characteristic temperature of transition into a metallic state T_{IMT} shifts toward high temperatures when La is replaced by a rare-earth ion with a smaller ionic radius. For example, we have $T_{\mathrm{IMT}} \approx 550$ K for $LaCoO_3$ and $T_{\mathrm{IMT}} \approx 800$ K for $GdCoO_3$. As noted above, the introduction of an element with a different ionic radius in a crystal lattice causes chemical pressure, which acts similarly to an external pressure. This is also true for a partial substitution. For example, the dielectric properties of compound $La_{1-x}Eu_xCoO_3$ are more pronounced when La is replaced by the Eu ion with a smaller ionic radius and concentration "x" increases.[39]

The large difference between the spin excitation gap Δ_S and the charge gap given by the activation energy for electrical conductivity E_g at low T indicates that perovskitelike rare-earth cobaltites are not simple band insulators.[33] Moreover, the discrepancy between the large charge gap and the T_{IMT} implies that the IMT can not be simply considered in terms of narrow-gap semiconductors.[20] Here, we solved this problem by calculating the electronic band structure in the regime of strong electron correlations within the multielectron LDA + GTB method.[22–24] We consider electron as the linear combination of quasiparticles (QP), so-called Hubbard fermions, given by excitations between the different multielectron configurations obtained by exact diagonalization of the CoO_6 cluster. The QP spectral weight is determined by the occupation numbers of the local multielectron states. For more details of the method, see Refs. 22–24, and 40.

To calculate the band dispersion in the strongly correlated material, one has to go beyond the local multielectron configuration. The natural tool to solve this problem is given by the Hubbard X operators X^{pq} constructed with the CoO_6 cluster eigenvectors $|p\rangle$ at site f. The X operator at site f is defined as

$$X_f^{pq} = |p\rangle\langle q|.$$

We write the Hamiltonian of a multiband p-d model in the form

$$H = H_d + H_p + H_{pd}^{\mathrm{hop}} + H_{pp}^{\mathrm{hop}} + H_{dd}^{\mathrm{Coul}}.$$

Here, the first two terms are responsible for the local one-electron energies of metal d electrons in the crystal field and anion p electrons, and the third term is p-d hopping (hybridization) t_{pd}. The term $H_{pp}^{\rm hop}$ is related to oxygen-oxygen hopping t_{pd}, and $H_{dd}^{\rm Coul}$ is the energy of the electrostatic interaction of electrons of a transition-metal ion. To take into account p-d hybridization and strong electron correlations, we divide the lattice into nonintersecting clusters (cells). The Hamiltonian of a multiband p-d model is written as

$$H = H_0 + H_1,$$

$$H_0 = \sum_f H_c(f),$$

$$H_1 = \sum_{f,g} H_{cc}(f,g),$$

where $H_c(f)$ is the intracell part of Hamiltonian H and $H_{cc}(f,g)$ describes the hopping and interaction between the fth and gth cells. Using a numerical exact diagonalization of intracell part $H_c(f)$, we find multielectron eigenstates $|m,N\rangle \equiv |p\rangle$ for various subspaces of the Hilbert space labeled by number N of electrons in a cell. All effects of the strong Coulomb interaction, spin-orbit coupling, covalency, and the crystal field inside the CoO_6 cluster are included in the set of the local eigenstates E_p. Here, p denotes the following quantum numbers: the number of electrons, spin S, and pseudo-orbital moment $\tilde{l}$ (or the total pseudomoment $\tilde{J}$ due to spin-orbit coupling), the irreducible representation in the crystal field. A relevant number of electrons is determined from the electroneutrality, for stoichiometric $GdCoO_3$ $N = 6$. The electronic-structure calculations require the electron addition and removal excitations. For $GdCoO_3$, it means the d^7 and d^5 configurations. The low-energy eigenstates are shown in Fig. 10. Here, $\underline{L}_{\sigma,\pi}$ is the spectroscopic notation of σ and π oxygen holes. To simplify the picture, the spin-orbit splitting is shown only for the high-spin state ${}^5T_{2g}$ d^6 configuration. Here, the energy-level notations are the same as in the ionic model, but there are some eigenstates containing the oxygen hole admixture due to the covalence effect. The calculation of the $N = 5,6,7$ eigenvectors for the CoO_6 cluster with the spin-orbit coupling and the Coulomb interaction has been done in Ref. 41. We assume that eigenstates $|p\rangle$ of neighboring cells are orthogonal. Otherwise (as in the case of cobaltites, where two neighboring CoO_6 clusters contain a common oxygen atom), an orthogonalization procedure should be used; that is, we have to construct a Wannier function in an explicit form instead of group oxygen orbitals. Such a procedure was first proposed for a three-band p-d model of cuprates[42] and was then generalized to a multiband model.[43] With the Hubbard operators constructed using the exact cluster eigenstates, we can calculate the QP band structure for the infinite lattice in the LDA + GTB approach. Following, we present the calculation results.

At temperature $T = 0$, only the ground term (low-spin singlet ${}^1A_1$) is populated in Co^{3+} ions in a $GdCoO_3$ crystal. The band structure is formed by the dispersion of the quasiparticle excitations in a multielectron system $d^6({}^1A_1) \to d^5(t_2^{52}T_2),(t_2^6\underline{L}_\pi{}^2T_2),(t_2^6\underline{L}_\sigma{}^2E)$ with the energies $\Omega_{V_1} = E(d^6,{}^1A_1) - E(d^5,t_2^{52}T_2)$, $\Omega_{V_2} = E(d^6,{}^1A_1) - E(d^5,t_2^6\underline{L}_\pi{}^2T_2)$, and $\Omega_{V_3} = E(d^6,{}^1A_1) - E(d^5,t_2^6\underline{L}_\sigma{}^2E)$, respectively, for the valence band, and $d^6({}^1A_1) \to d^7({}^2E)$ for the conduction band with the energy $\Omega_C = E(d^7,{}^2E) - E(d^6,{}^1A_1)$ (Fig. 10, solid lines) due to the intercell hopping. The excitation energies determine the positions of the band centers. Obviously, the bands Ω_V and Ω_C are analogs of the lower and upper Hubbard subbands in the Hubbard model. In general, Fig. 10 looks similar to Fig. 6 of Ref. 34. To explain our methodology more clearly, here we have shown separately the different contributions to the d^5 eigenstates, the pure ionic configuration d^5p^6 of Co^{3+} and O^{2-}, and the ligand hole d^6p^5 configuration. The QP band structure corresponds to the charge-transfer insulator[44] with a temperature-dependent insulator gap E_g. The $GdCoO_3$ band structure at $T = 0$ is shown in Fig. 11.

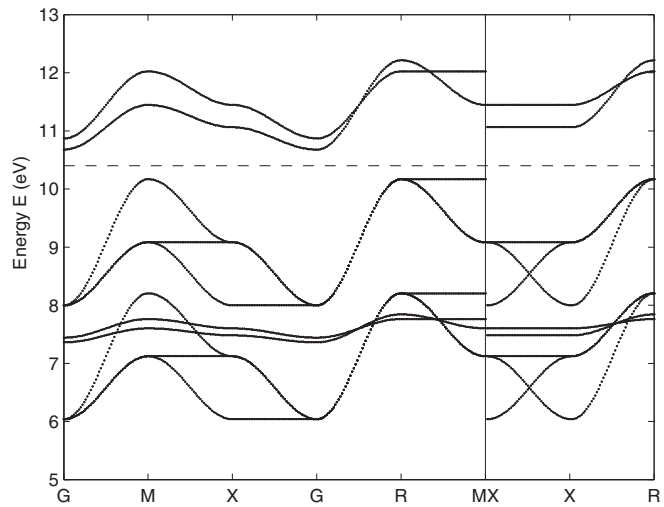

FIG. 11. Quasiparticle spectrum at $T = 0$. $GdCoO_3$ is the charge-transfer insulator with the energy gap $E_g \approx 0.5$ eV. $G(0,0,0)$, $M(\pi,\pi,0)$, $X(\pi,0,0)/(0,\pi,0)$, $R(\pi,\pi,\pi)$ are symmetric points of the Brillouin zone. More/less dark color of the dispersion curves corresponds to the more/less quasiparticle spectral intensity. High intensity appears when several bands degenerate.

The general property of the Hubbard fermions is a strong dependence of the QP spectral weight on the occupation numbers of the initial and final multielectron terms for the given excitation. It is clear that the excitation from empty-to-empty terms has zero spectral weight. That is why nonzero spectral weight at $T = 0$ is related to the participation of the occupied LS Co^{3+} term; all possible excitations are shown in Fig. 10 by solid lines. The excitations between LS d^6 and HS d^5 terms are forbidden by the spin conservation law (spin blockade according to Khomskii).

When temperature increases, the quasiparticle spectrum undergoes substantial changes: the thermal population of sublevels $\tilde{J} = 1$, 2, and 3 of the ${}^5T_2$ term increases, resulting in contributions from possible excitations allowed by the selection rules for spin and spin projection ($\Delta S = \pm 1/2$, $\Delta S_Z = \pm 1/2$). The $d^6({}^5T_2) \to d^5[t_2^3({}^4A_2)e^2({}^3A_2){}^6A_1]$, $\{[t_2^4({}^3T_1)e^2({}^3A_2)]^5T_2\underline{L}_\pi{}^6A_1\}$ transitions shown as the dashed lines in Fig. 10 with energies $\Omega^*_{V_1}$ and $\Omega^*_{V_2}$ are responsible for the appearance of in-gap states (excitations that are

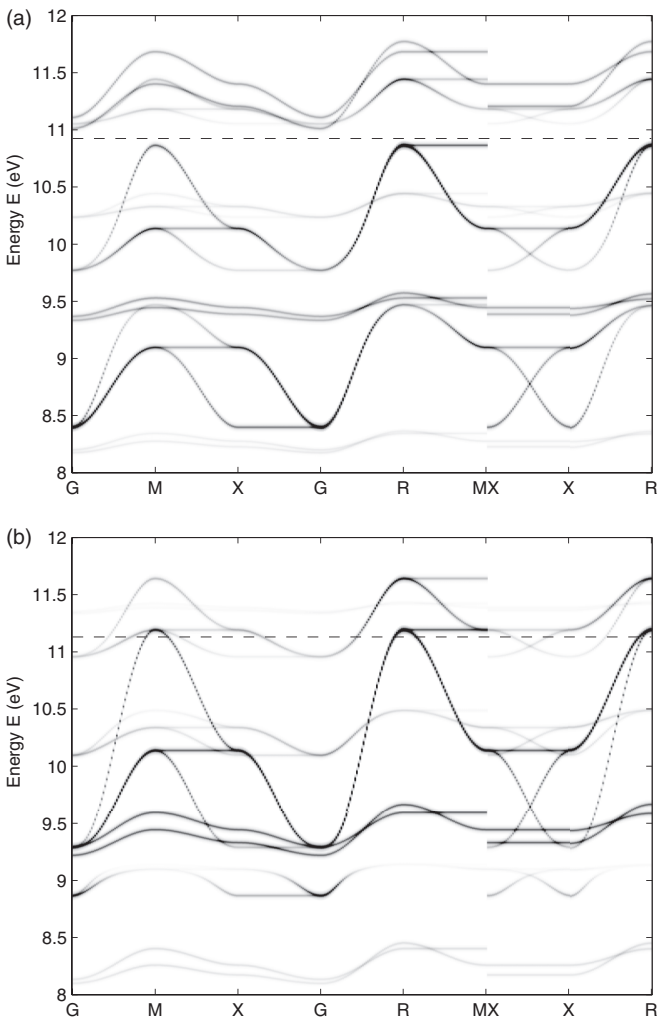

FIG. 12. Effect of HS thermal population on quasiparticle spectrum at high temperature. (a) At $T = 750$ K, the in-gap states are observed both near the chemical potential level and inside the bands; (b) at $T = 800$ K, the band structure is of the semimetal type with electrons and holes at the chemical potential. The dashed line shows the chemical potential.

higher in energy than Ω_{V_1}, Ω_{V_2}, and Ω_{V_3} but lower than Ω_C) and for the insulator gap decrease. For each temperature, the chemical potential and the QP band structure are calculated self-consistently. The QP band structures for $T = 750$ and 800 K are shown in Fig. 12. The spectral weight and the in-gap bandwidth are proportional to the population of sublevels $\tilde{J} = 1$ and 2 of a high-spin state. An increase of temperature leads to the fact that the bands formed by the transitions $d^6(^5T_2) \rightarrow d^5[t_2^3(^4A_2)e^2(^3A_2)^6A_1]$, $\{[t_2^4(^3T_1)e^2(^3A_2)]^5T_2\underline{L}_\pi{}^6A_1\}$, and $d^6(^5T_2) \rightarrow d^7(^4T_1)$ begin increasing the width, and the insulator gap decreases. The quasiparticle spectrum and the insulator gap E_g are determined by the thermal population of the HS state and, hence, by the spin gap Δ_S. Due to the temperature dependence Δ_S in $GdCoO_3$, the insulator gap E_g vanishes as temperature increases at $T_{\mathrm{IMT}} \approx 780$ K [Fig. 12(b)]. Figure 13 shows the temperature dependence of the insulator band gap in $GdCoO_3$. We also plotted in Fig. 13 the heat capacity measured for our $GdCoO_3$ samples to demonstrate that a smooth maximum in

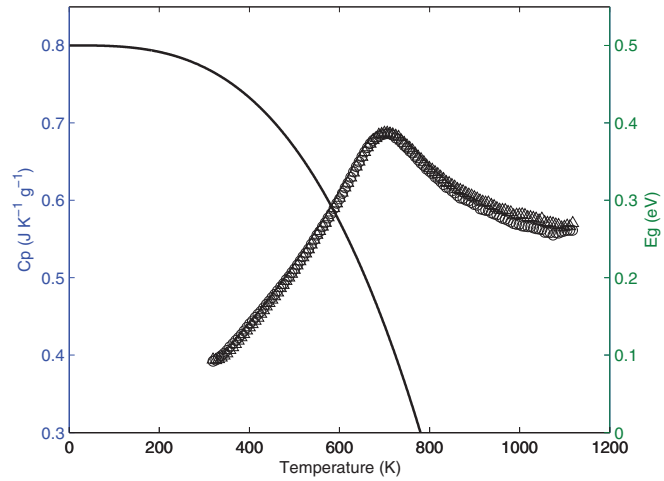

FIG. 13. (Color online) Temperature dependence of measured heat capacity and calculated insulator band gap E_g; $E_g = 0$ at $T = T_{\mathrm{IMT}} \approx 780$ K. Experimental data have been measured for solid-state synthesized (triangles) and sol-gel (circles) samples.

the C_P temperature dependence is related to the insulator-metal transition. Both are smooth due to strong thermal fluctuations of electrons above the small insulator gap in the vicinity of T_{IMT}.

The results of calculations of the $GdCoO_3$ band structure were given earlier in Ref. 34, where the spin gap was considered fixed for all temperatures $\Delta_S \approx 2000$ K. The temperature dependence of the spin gap leads to the significant changes in the $GdCoO_3$ band structure with increasing temperature because the spectral weight of in-gap quasiparticle excitations is determined by the thermal population of the HS state. Thus, in Ref. 34 the band structure was of insulator type for all temperatures, while here due to the spin crossover we have obtained the insulator-metal transition at $T_{\mathrm{IMT}} \approx 780$ K.

VIII. CONCLUSIONS

Previously, the effect of HS-LS fluctuations has been studied in detail for $LaCoO_3$, and several publications[11,13,21] concern the structural, magnetic, thermodynamic, and electronic properties of $GdCoO_3$ and similar rare-earth perovskites. The analysis of high-precision XRD data allowed detecting the phase separation of two different spin states in $GdCoO_3$ at a finite temperature interval (Fig. 4). The *ab initio* DFT-GGA calculations of the $GdCoO_3$ total energy in different possible spin states allows relating the phase separation to the coexistence of the HS and LS states. The key parameter for the HS/LS balance is the spin-gap value. At low temperatures, it is large due to the chemical pressure effect resulting from the La $\rightarrow$ Gd substitution, the spin gap being more than 2000 K at 0 T. At first glimpse, all thermal excitations in a material with such large spin gap may be expected only at very high $T \sim 1000$ K. Nevertheless, the anomalously large thermal expansion (negative pressure) results in the decreasing spin gap. To find the temperature-dependent spin gap, we have carried out the magnetic measurements up to 900 K. At high temperature, the large paramagnetic Gd^{3+} susceptibility is strongly suppressed and small Co^{3+} susceptibility from the

thermally excited HS state can be reliably measured. Fitting the Co^{3+} susceptibility based on the partition function for the multielectron energy-level scheme provides us with the temperature-dependent spin gap. Its value and temperature dependence appear to be close to the gap found earlier in Ref. 11.

Zero spin gap at temperature T_S means the spin crossover between the LS and HS states of the Co^{3+} ions. Usually, spin crossover in transition-metal oxides from HS to LS is induced by external high pressure.[45] In $GdCoO_3$ we found the inverse crossover from the LS to HS state resulting from the thermal expansion (negative pressure). In the two-phase model with HS/LS probabilities calculated with the found spin gap and the LS and HS volumes calculated by DFT-GGA, we were able to reproduce the temperature dependence of the unit-cell volume and thermal expansion. Thus, the qualitative agreement of the calculated structural parameter [unit-cell volume in Fig. 9(b)] with the experimental one confirms the model of temperature-dependent spin gap based on magnetic measurements. Finally, we conclude that in $GdCoO_3$ the main mechanism of the lattice expansion is not the conventional lattice anharmonicity, but the HS/LS fluctuations. The large (about 10%) difference in the HS and LS ionic radii makes it clear why spin-state fluctuations may result in the lattice expansion.

The possible contribution of the IS state of Co^{3+} was a challenging question. At low T, it is clear from the crystal-field theory that the IS term lies well above the LS term. Nevertheless, it was not obvious how the effect of negative pressure induced by strong thermal expansion may change the stability of the IS state. We have resolved this question by the modified crystal-field approach. The IS-LS excitation energy is reduced with heating [Fig. 7(b)] being more 6000 K up to the $T \sim 1000$ K. This conclusion allows excluding a significant contribution of the IS state to all studied here properties.

As for the electronic properties of $GdCoO_3$, the strong electron correlations hinder standard single-electron band theory methods and require the multielectron approach. We use here the LDA + GTB method developed earlier for high-temperature superconducting cuprates[22,23] and applied recently to $LaCoO_3$.[10] At zero temperature, we have obtained the charge-transfer insulator. We have found that the thermal population of different sublevels of the $^5T_{2g}$ HS term results both in the spin-state transition and also in some new QP excitations. Of particular importance is the hole creation QP from the initial d^6 HS into the d^5 HS terms. This QP at finite temperature appears to form the in-gap state inside the large charge-transfer gap. The intercell hopping transforms this local QP into the in-gap band that lies just under the bottom of the empty conductivity band. Its bandwidth increases with T, and the insulator-metal smooth transition occurs due to the overlapping with the conductivity band at $T = T_{\mathrm{IMT}} \approx 780$ K. The heat capacity measured for our $GdCoO_3$ samples and plotted in Fig. 13 demonstrates that a smooth maximum in the C_P temperature dependence is related to the insulator-metal transition. Both are smooth due to strong thermal fluctuations of electrons above the small insulator gap in the vicinity of T_{IMT}.

Finally, we want to emphasize that the spin value fluctuations considered here should not be understood as spin fluctuations. The latter usually means fluctuations of the spin projection. Many years ago, Vonsovskii introduced a term "multiplicity fluctuations" to discuss a variation of the magnitude of the spin in the d shell.[47] We consider this term the more precise and relevant for the HS/LS fluctuations. The microscopic mechanism of the ionic radius change at the multiplicity fluctuation has been discussed in Ref. 48.

ACKNOWLEDGMENTS

The authors are thankful to I. S. Edelman and R. S. Iskhakov for useful discussions, and M. S. Molokeev for technical support. The authors acknowledge financial support by the President of Russia Grant No. NSh-1044.2012.2, Presidium of RAS (Project No. 20.7), Siberian Branch of Russian Academy of Sciences (Projects No. 38 and No. 44), RFBR Grants No. 12-02-90410, No. 12-02-00175, No. 12-02-31543, No. 13-02-00358, No. 13-02-00958, No. 13-02-01395, Ministry of Education and Science of the Russian Federation (state Contract No. 16.740.12.0731), Siberian Federal University Grant F-11, Grant of President of Russia, Project No. MK1168.2012.2, Grant No. 27-02-12 of National Academy of Sciences of Ukraine and the Russian Foundation for Basic Research also by the Grant NAS of Ukraine 91/13-H.

*sgo@iph.krasn.ru

[1] S. Maekava, T. Tohyama, S. E. Barnes, S. Ishihara, W. Koshibae, and G. Khaliullin, *Physics of Transition Metal Oxides* (Springer, Berlin, 2004).
[2] J. B. Goodenough, J. Phys. Chem. Solids **6**, 287 (1958).
[3] C. Zobel, M. Kriener, D. Bruns, J. Baier, M. Gruninger, T. Lorenz, P. Reutler, and A. Revcolevschi, Phys. Rev. B **66**, 020402 (2002).
[4] T. Kyomen, Y. Asaka, and M. Itoh, Phys. Rev. B **67**, 144424 (2003).
[5] J.-Q. Yan, J.-S. Zhou, and J. B. Goodenough, Phys. Rev. B **69**, 134409 (2004).
[6] S. Stolen, F. Gronvold, H. Brinks, T. Atake, and H. Mori, Phys. Rev. B **55**, 14103 (1997).
[7] S. Noguchi, S. Kawamata, K. Okuda, H. Nojiri, and M. Motokawa, Phys. Rev. B **66**, 094404 (2002).
[8] M. W. Haverkort, Z. Hu, J. C. Cezar, T. Burnus, H. Hartmann, M. Reuther, C. Zobel, T. Lorenz, A. Tanaka, N. B. Brookes, H. H. Hsieh, H.-J. Lin, C. T. Chen, and L. H. Tjeng, Phys. Rev. Lett. **97**, 176405 (2006).
[9] Z. Ropka and R. J. Radwanski, Phys. Rev. B **67**, 172401 (2003).
[10] S. G. Ovchinnikov, Yu. S. Orlov, I. A. Nekrasov, and Z. V. Pchelkina, J. Exp. Theor. Phys. **112**, 140 (2011).
[11] K. Knizek, J. Jirak, J. Hejtmanek, M. Veverka, M. Marysko, G. Maris, and T. T. M. Palstra, Eur. Phys. J. B **47**, 213 (2005).
[12] S. G. Ovchinnikov, Yu. S. Orlov, and V. A. Dudnikov, J. Magn. Magn. Mater. **324**, 3584 (2012).
[13] M. Tachibana, T. Yoshida, H. Kawaji, T. Atake, and E. Takayama-Muromachi, Phys. Rev. B **77**, 094402 (2008).
[14] E. Blochl, Phys. Rev. B **50**, 17953 (1994).
[15] G. Kresse and J. Hafner, Phys. Rev. B **49**, 14251 (1994).

[16]G. Kresse and J. Furthmuller, Phys. Rev. B **54**, 11169 (1996).
[17]D. Vanderbilt, Phys. Rev. B **41**, 7892 (1990).
[18]J. P. Perdew, K. Burke, and M. Ernzerhof, Phys. Rev. Lett. **78**, 1396 (1997).
[19]H. J. Monkhorst and J. D. Pack, Phys. Rev. B **13**, 5188 (1976).
[20]S. Yamaguchi, Y. Okimoto, and Y. Tokura, Phys. Rev. B **54**, R11022 (1996).
[21]B. Scherrer, A. S. Harvey, S. Tanasescu, F. Teodorescu, A. Botea, K. Conder, A. N. Grundy, J. Martynczuk, and L. J. Gauckler, Phys. Rev. B **84**, 085113 (2011).
[22]M. M. Korshunov, V. A. Gavrichkov, S. G. Ovchinnikov, Z. V. Pchelkina, and I. A. Nekrasov, J. Exp. Theor. Phys. **99**, 559 (2004).
[23]M. M. Korshunov, V. A. Gavrichkov, S. G. Ovchinnikov, I. A. Nekrasov, Z. V. Pchelkina, and V. I. Anisimov, Phys. Rev. B **72**, 165104 (2005).
[24]V. A. Gavrichkov, S. G. Ovchinnikov, I. A. Nekrasov, and Z. V. Pchelkina, J. Exp. Theor. Phys. **112**, 860 (2011).
[25]H. M. Rietveld, J. Appl. Crystallogr. **2**, 65 (1969).
[26]L. A. Solovyov, J. Appl. Crystallogr. **37**, 743 (2004).
[27]N. B. Ivanova, N. V. Kazak, C. R. Michel, A. D. Balaev, and S. G. Ovchinnikov, Phys. Solid State **49**, 2126 (2007).
[28]V. A. Dudnikov, D. A. Velikanov, N. V. Kazak, C. R. Michel, J. Bartolome, A. Arauzo, S. G. Ovchinnikov, and G. S. Patrin, Phys. Solid State **54**, 79 (2012).
[29]See Supplemental Material at http://link.aps.org/supplemental/10.1103/PhysRevB.88.235105 for Crystallographic information file for $GdCoO_3$.
[30]P. G. Radaelli and S.-W. Cheong, Phys. Rev. B **66**, 094408 (2002).
[31]M. J. R. Hoch, S. Nellutla, J. van Tol, E. S. Choi, J. Lu, H. Zheng, and J. F. Mitchell, Phys. Rev. B **79**, 214421 (2009).
[32]T. Vogt, J. A. Hriljac, N. C. Hyatt, and P. Woodward, Phys. Rev. B **67**, 140401(R) (2003).
[33]S. Yamaguchi, Y. Okimoto, H. Taniguchi, and Y. Tokura, Phys. Rev. B **53**, R2926 (1996).
[34]V. A. Dudnikov, S. G. Ovchinnikov, Yu. S. Orlov, N. V. Kazak, C. R. Michel, G. S. Patrin, and G. Yu. Yurkin, J. Exp. Theor. Phys. **114**, 841 (2012).
[35]E. S. Zhitlukhina, K. V. Lamonova, S. M. Orel, P. Lemmens, and Yu. G. Pashkevich, J. Phys.: Condens. Matter **119**, 156216 (2007).
[36]R. Yu. Babkin, V. Lamonova, S. Orel, and Yu. G. Pashkevich, Opt. Spectrosc. **107**, 9 (2009).
[37]K. Lamonova, E. Zhitlukhina, R. Babkin, S. Orel, S. Ovchinnikov, and Yu. Pashkevich, J. Phys. Chem. **115**, 13596 (2011).
[38]S. Sugano, Y. Tanabe, and H. Kamimura, *Multiplets of Transition-Metal Ions in Crystals* (Academic, New York, 1970).
[39]J. Baier, S. Jodlauk, M. Kriener, A. Reichl, C. Zobel, H. Kierspel, A. Freimuth, and T. Lorenz, Phys. Rev. B **71**, 014443 (2005).
[40]S. G. Ovchinnikov, V. A. Gavrichkov, M. M. Korshunov, and E. I. Shneyder, in *Theoretical Methods for Strongly Correlated Systems*, edited by A. Avella and F. Mancini, Springer Series in Solid-State Sciences (Springer, Berlin, 2012), Vol. 171, pp. 143–171.
[41]Yu. S. Orlov and S. G. Ovchinnikov, J. Exp. Theor. Phys. **109**, 322 (2009).
[42]F. C. Zhang and T. M. Rice, Phys. Rev. B **37**, 3759 (1988).
[43]L. F. Feiner, J. H. Jefferson, and R. Raimondi, Phys. Rev. B **53**, 8751 (1996).
[44]J. Zaanen, G. A. Sawatzky, and J. W. Allen, Phys. Rev. Lett. **55**, 418 (1985).
[45]I. S. Lyubutin and A. G. Gavriliuk, Phys. Usp. **52**, 989 (2009).
[46]I. B. Bersuker, *Electronic Structure and Properties of Transition Metal Compounds: Introduction to the Theory* (Wiley, Hoboken, NJ, 1996).
[47]S. V. Vonsovskii and M. S. Svirskii, ZhETF **47**, 1354 (1965) [J. Exp. Theor. Phys. **20**, 914 (1965)].
[48]I. S. Sandalov and V. I. Filatjev, Phys. B (Amsterdam) **162**, 139 (1990).